

Contents lists available at ScienceDirect

Structures

journal homepage: www.elsevier.com/locate/istruc



Improving damage detection in masonry bridges: A combination of finite–discrete element method and genetic algorithms

R. Bravo^{a,*} , J.L. Pérez-Aparicio^b

- a University of Granada, Department of Structural Mechanics and Hydraulic Engineering, Campus de Fuentenueva S/N., Granada, 18071, Spain
- b Universitat Politècnica València, Department of Continuum Mechanics & Structures, Camino de Vera S/N, Valencia, 46022, Spain

HIGHLIGHTS

- Parametric Finite Discrete Element Methods allow accurate study of masonry structures.
- Block contact and friction are necessary for the new inverse problem of damage location.
- Combination of Finite-Discrete and Genetic methods has not been applied to masonry.
- Random noise must modify initial numerical data to simulate real structural results.
- Finding 1 or 2 blocks is accurate in most cases although dependent on noise.

ARTICLE INFO

Keywords: Masonry structures Discrete elements Genetic algorithm Inverse problem Damage detection

ABSTRACT

Thousands of masonry structures are part of the international railway and road networks, with some remaining in use for up to two centuries. Given increasing operational demands in both traffic weight and speeds, developing effective damage detection techniques becomes essential for their proper maintenance. Currently, damage assessment is performed primarily in situ, involving a high costs. Therefore, a numerical tool based on an inverse problem for damage detection from a series of indirect and/or permanent measurements is necessary. As a first step, this paper presents a numerical approach that combines finite and discrete element methods with genetic algorithms to identify the position of one or two missing blocks in a one–span masonry bridge. Field measurements are replaced with a displacement set from a two–dimensional FemDem mesh considering missing blocks. These numerical distributions are sampled at a limited number of control nodes and are perturbed with statistical noise to simulate the variations in the actual measurements. The results are compared with a small population of new numerical cases generated by the genetic algorithm. With appropriate noise levels, it is demonstrated that the method can find the missing locations automatically and accurately identify the missing locations.

1. Introduction

Masonry arches made out of adobe bricks can be traced back to 3000 years BC in ancient cultures [1]; the advantage of this particular geometry is that it transforms the bending stresses of straight beams into purely compressive stresses. During Roman times, the application of arches evolved from habitational buildings to infrastructures such as bridges and aqueducts or even domes in their three–dimensional (3D) version. The preferred materials became, as they are today, fired brick or stone.

Among the infrastructures, the masonry bridge is one of the oldest structural typologies due to its ease of construction, the availability of rock material in the surrounding areas, and the high capacity of the stone to work under compression. Thus, these structures present high resistance and stiffness, and they have a significant durability that has permitted their survival over centuries. Nowadays, a vast structural heritage needs to be preserved, and many of these bridges are still in service: there could be over 22,000 in Europe alone, and even more in other continents.

Most functioning masonry bridges are part of public transportation systems, constructed between the 19^{th} and mid- 20^{th} centuries. Adapting them to new structural operational conditions is necessary since they

^{*} Corresponding author.

Email address: rbravo@ugr.es (R. Bravo).

support axial loads higher than initially predicted; therefore, new and more accurate tools are required for their analysis.

Since masonry bridges are composed of stones or bricks glued by mortar or directly in contact, they are internally discontinuous structures, [2]. Contact provides the structure's overall stability; as a consequence, complex nonlinear and discontinuous behavior appears as explained in [3]. Early efforts to investigate the behavior of arches can be traced back to the first experimental studies of the Roman architect Vitruvius in the 1st century B.C. [4]. Many years later, the Renaissance engineer and artist Leonardo da Vinci [5] focused on stability analysis to design a 240 m single–span masonry bridge (without mortar) over the Golden Horn, Istanbul.

Comprehensive graphical methods were developed in the XIX century [6] for calculating discontinuous structures. Later, semiempirical methods [7], analytical formulations [8], or methods based on linear and nonlinear elasticity [9] emerged. These methods can often accurately model the nonlinear behavior, but only apply to the simplest geometries and loads. Therefore, there is a need to consider advanced techniques that account for the masonry's inherent structural discontinuous nature.

The Discrete Element Method (DEM) [10] is a numerical tool capable of calculating the response of multibody systems interacting through contact and friction, and it was first implemented in the 1970 s. DEM modelling of masonry structures is of natural and immediate application [11,12]. Moreover, applying DEM to analyze a wide range of historical masonry structures is possible thanks to the current increase in computational capabilities. These structures include walls [13–16], arches [17,18], masonry columns [19], buildings under static and dynamic regimes [20] or domes in 3D static/dynamic situations [21].

Methods similar to DEM, such as Non–Smooth Contact Dynamics, have been published in [22]; however, their application requires a significantly high computational cost. The Finite Element Method (FEM) is an alternative, but inserting interfaces for the contact between blocks makes it less competitive, [23–25]. Despite the suitability of DEM to represent rigid body mechanics, its accuracy for internal strains and stresses inside the block is lower than that of FEM, [26]. A comprehensive review of analytical and numerical methods for assessing the performance of masonry structures can be found in [27].

The combination of DEM to model the interactions between blocks and FEM to model their elasticity is optimal for studying the mechanical behavior of masonry structures. This fusion is known as the combined Finite–Discrete Element Method (FemDem) [28], which has gained widespread application in recent years, [29]. It has also become a powerful tool in the fields of rock and geo–mechanics [30]. More recently, [31] has shown how this combination can also be helpful for structural engineering, as in the study of the collapse of masonry arches under various static actions. The extension to cases with dynamic loads has been made for simple structures, such as walls under cyclic loads [32].

Identifying structural deterioration is essential for adequately evaluating and maintaining masonry structures. Direct visual inspection remains the standard practice for detecting structural deterioration. However, it is usually restricted to the external parts of the bridge. Destructive testing methods consist of small penetration/extraction techniques of specimens that only partially assess the structure; moreover, they are only suitable for use in preliminary inspections.

In addition to traditional inspection and monitoring techniques, more advanced—though often costly—approaches such as Nondestructive Testing (NDT) can provide a detailed assessment of a bridge's structural condition. Using sensors or imaging technologies, these methods can monitor the onset of damage, crack formation, and large deformations [33], supplying valuable data to prevent structural pathologies. Comprehensive reviews of NDT applications are provided in [34,35], while [36] focuses on Acoustic Emission techniques. Experimental approaches based on ambient vibration testing and operational modal analysis have been reported in [37,38], along with methods combining ambient and random impact vibrations. Recent developments also include the use of self-sensing materials for new

masonry structures [39] and advanced methods based on deep learning and image reconstruction [40,41].

Several studies combine structure monitoring with FEM simulations, as previously mentioned, while FEM can model discontinuous domains through interface elements, this approach becomes computationally less competitive for masonry structures with numerous contact interfaces [42]. DEM has been used with inverse or optimization algorithms involving interactions between bodies. Some examples are the calibration of microparameters in granular materials using Genetic Algorithms (GA) [43], a specialized heuristic optimization tool that relies on the application of the rules of both natural selection and genetics [44], the identification of rock–like material parameters [45], and the shape optimization of bucket elevators [46]. However, to the best of our knowledge, existing literature lacks numerical procedures based on DEM or FemDem specifically designed for damage detection in masonry structures exhibiting discontinuities between blocks.

This paper presents an inverse method for damage location in a masonry bridge using FemDem. A brief description of FemDem and a numerical parametric model of a masonry arch bridge missing one or two blocks will be developed in Section 2; a similar bridge has been studied in [47] for other objectives. Also, an objective function, built upon the numerical displacements of the bridge contour, is proposed in Section 3. This function is minimized using a GA capable of finding the missing blocks' location. Since experimental displacements are currently unavailable and no direct experimental analog was found in the literature, they will be simulated by direct "experimental" FemDem simulations in which the positions of the missing blocks are known; subsequently, the inverse problem will detect these positions without the initial information. Although the lack of experimental data represents a limitation of the current study, this work constitutes a critical phase before proceeding to physical validation as it is well-established in the literature on structural health monitoring of historical masonry [48,49]. Different noise levels will be inserted into the "experimental" displacements to account for possible interferences from monitoring systems or surrounding effects in actual experiments. This methodology provides insight into the proposed method's ability to detect damage for different noise levels and for the cases and results presented and discussed in Sections 4 and 5.

2. The FemDem method, masonry bridge model and parameters

The modelling strategy adopted is based on the combined Finite Element–Discrete Element Method, which has been extensively used in the analysis of masonry structures due to its capability to represent both the continuum mechanical behavior of the blocks and the discrete nature of the joints [11,28]. This hybrid approach integrates the strengths of the Finite Element Method for accurately computing stresses and strains within each block, with those of the Discrete Element Method for modelling contact interaction, separation, sliding, and rotation between blocks.

In the FemDem framework, each masonry unit is discretized into finite elements connected by cohesive interfaces representing the mortar joints. Contact detection algorithms are employed to identify potential interactions between adjacent blocks when relative displacements occur. Once contact is detected, normal and tangential contact laws govern the transfer of forces, incorporating stiffness degradation and frictional sliding where relevant. This formulation naturally handles nonlinear phenomena such as crack initiation at joints, progressive joint opening and closing, and post–peak softening. Moreover, the method can reproduce large displacements and rotations without the numerical instabilities that can affect purely continuum-based models.

While masonry bridges are 3D structures, the dimension perpendicular to the main plane is smaller than the others; this two-dimensional (2D) assumption is more evident in early railroad bridges with only one track. Furthermore, most loads act within the frontal plane, resulting in minimal out-of-plane displacements. The current 2D model,

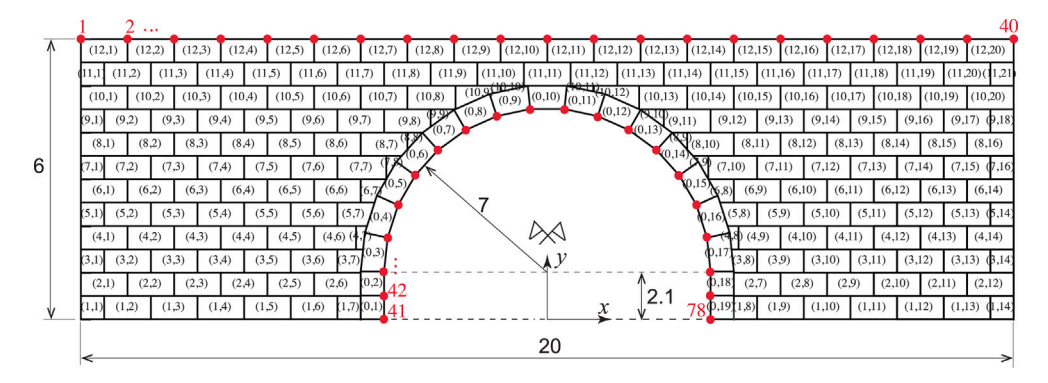


Fig. 1. Geometry of the masonry bridge. A pair of integers (x_1, x_2) identifies each block. Control points for displacement δ are numbered in red.

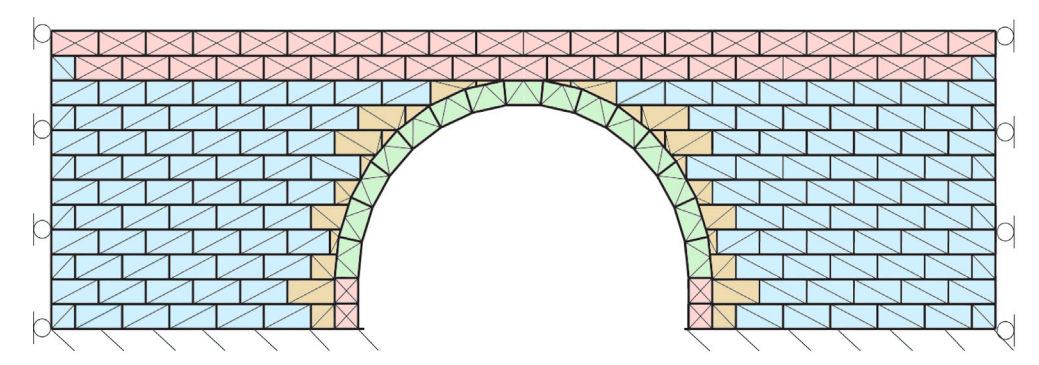


Fig. 2. Symmetric FemDem masonry bridge mesh, indicating the boundary conditions and discretization of block in two (blue), three (green), four (pink) and variable (brown) finite elements.

see Fig. 1, neglects the fill material due to its relatively lower stiffness compared to the stone masonry. Therefore, the geometry resembles a plane stress/strain situation. This simplification is appropriate for the initial development of the damage detection methodology, as the primary structural response is governed by the arch and spandrel walls, see [31]. For practical applications requiring higher accuracy, the model can be extended to include fill properties through equivalent stiffness adjustments [50] or 3D modelling [51].

As mentioned, the objective of the current article is to develop and apply an algorithm to automatically detect the absence of some blocks in a structure, comparing the behavior of a base case that simulates experimental measurements with other cases missing one or two blocks. Both cases are evaluated on the reference masonry bridge illustrated in Fig. 1, consisting of a semicircular arch with external dimensions of 20 m (span) by 6 m (rise). The arch has a radius of R=7 m, with its center located on the vertical axis of symmetry at a height of 0.3 R above ground level. Location of blocks is indexed by a pair of coordinates, and vertical displacements used in this work are recorded at the control points indicated by red dots.

For this purpose, a FemDem mesh corresponding to the blocks of the figure is created, see Fig. 2. It is composed of 212 rectangular blocks of general dimensions 1×0.5 m with 529 elements. The exception is for the transition blocks close to the arch, whose shape and size have been adapted to accommodate the intersections with the arch, mimicking real-world masonry construction. As each block is identified by a pair of indices (see Fig. 1; therefore, the locations and the absence of one or more blocks in the inverse problem can be easily registered. The bridge's motion is prevented at its base (clamped), and the lateral sides can move vertically to simulate the rest of the terrain. To mimic real structural inspections and leverage their accessibility, the red nodes located in the arch intrados and on the upper side of the bridge are designated as control points for measuring vertical displacements in the inverse problem.

FemDem is a computationally demanding method, with runtime dependent on the number of contact interfaces and the internal discretization of each block. To achieve a reasonable CPU time with good accuracy and a robust simulation in contact scenarios, see Munjiza in [28], the discretization is performed with triangular finite elements (FE), as shown in Fig. 2 as follows:

- (a) The rectangular blocks at the lateral sides of the bridge are divided into two FE since their mechanical behavior is quite homogeneous (blue).
- (b) The arch blocks are divided into three FE due to their significant stress gradient (green).
- (c) At the arch bottom and the bridge's highest row—where the stresses are highly concentrated—they are divided into four FE (pink).
- (d) The transition blocks are divided into one to three FE to maintain a good aspect ratio (brown).

The mechanical and numerical parameters adopted in the model are summarized in Table 1. The notation is as follows: E denotes the Young's modulus, ν the Poisson's ratio, ρ the density, p_n and p_t the penalty parameters in the normal and tangential directions, respectively, and ϕ the friction angle between blocks. Most of the mechanical parameters are obtained from Ref. [52]; however, p_n and p_t are computed according to the prescriptions in Ref. [28].

Table 1Mechanical and numerical material parameters of the FemDem model.

E	ν	ρ	p_n	p_t	φ
N/m ²	-	kg/m ³	N/m	N/m	۰
2.5e10	0.2	2400	1e9	1e8	35

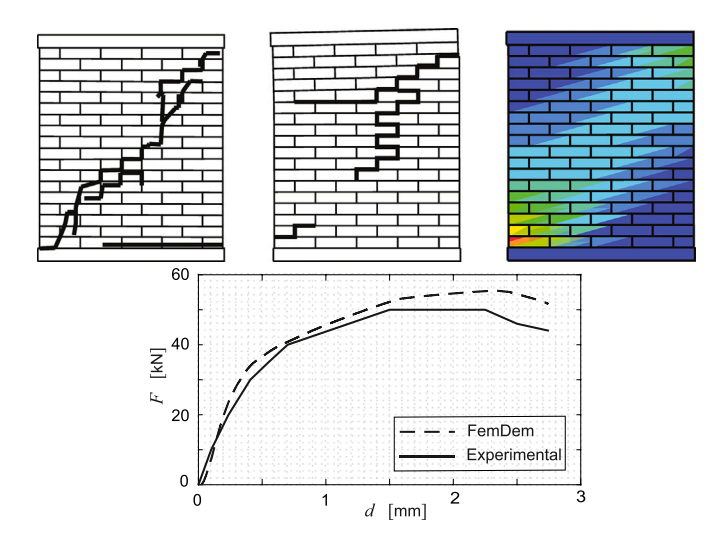


Fig. 3. (Top). Eindhoven wall, experimental crack progress, left; FemDem crack progress, center; Tresca stress, right; red maximum with a blue minimum of 0. (Bottom) Displacement *d* vs. reaction force *F* at the top nodes.

The blocks are assumed to be homogeneous stones with very high compressive strength. Therefore, they cannot fracture; their surfaces are rough without mortar in joints (dry stone).

Although the present study does not reproduce an experimental test directly, the modelling approach has been contrasted with relevant experimental evidence from the literature. In particular, the Eindhoven masonry wall experiment [52,53] provides a valuable reference for validating the general mechanical behavior captured by the FemDem formulation. This large-scale test involved a masonry wall subjected to lateral mechanical loading and monitored under controlled laboratory conditions, see Fig. 3. These validation results were previously published by the authors in [47]. In this setup, contact discontinuities naturally occurred due to load-induced cracking and detachment, where the results (crack openings) produced by FemDem, Fig. 3 (top-left), fit well with the experimental results (top-center). Additionally, a numerical representation of the Tresca stress is presented. The numerical and experimental displacement d vs. reaction force F relations shown in Fig. 3 bottom, show a good agreement, confirming that the model accurately reproduces the physical behavior. The slight discrepancy observed at the end of the distribution (approximately 19 % compared to the experiment) can be attributed to the model's limitations in capturing internal brick failure. These parallels support the capability of the numerical model to reproduce realistic structural responses, thereby reinforcing confidence in its application to the detection of block-scale damage in masonry bridges.

3. Inverse problem description and methodology

This section presents the inverse problem of damage identification formulated with FemDem to locate missing block positions. The corresponding objective function is calculated using the distribution of vertical displacements δ under the gravity of the bridge for the control points shown in Fig. 1. These displacements are computed parametrically as a function of the positions of the missing blocks, identified with the pair of integer indices (x_1, x_2) defined in Fig. 1.

The present work is exclusively computational. Therefore, instead of using real experimental displacements, numerical displacements $\delta^{ex}(x_1,x_2)\equiv\delta^{ex}$ at the control nodes of Fig. 1 from a direct FemDem case (in which one or two blocks are missing) are used as reference. The superscript "experimental" is only symbolic, indicating that numerical data takes the place of experimental data.

To replicate the inherent variations in field measurements, noise is added to the δ^{ex} data. The noise is uniformly applied to all displacements

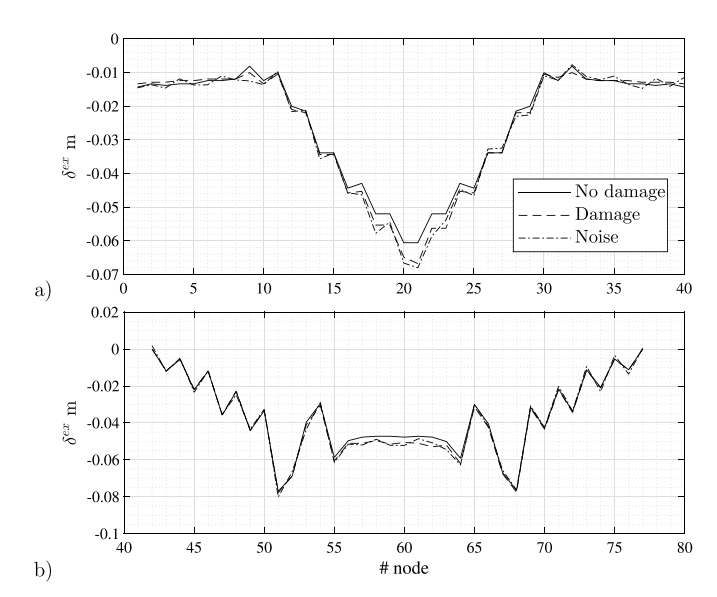


Fig. 4. Vertical FemDem displacements at control nodes: (a) top row and (b) arch, for both the intact structure (No damage) and the damaged case with block (10,4) removed (see Fig. 1), presented without noise (Damage) and with 14 % roise.

and its amplitude is user—chosen from 5 % to 10 %. The higher the noise, the more difficult it is for GA to converge since the "experimental" distribution becomes very different from that of the FemDem, the objective function is high, and the minima may be found at incorrect locations.

As a preliminary example, Fig. 4 shows the numerically calculated δ^{ex} with FemDem for the case without damage (continuous line), and the particular case of the missing block $(x_1, x_2) = (10,4)$, without (dashed line) and with a 14 % noise (dash-dotted line). For blocks at the top row of the bridge numbered 1 to 40, the figure a) shows that the values are slightly higher at the center-left due to the lower rigidity induced by the missing block. The figure b) plots the δ^{ex} of the arch; the distribution is now almost symmetric since the missing block does not affect the arch displacements much, and its absolute maximum value lies close to the central keystone. The results with and without noise are similar (though not identical) because the 14 % noise is applied only to the total δ^{ex} standard deviation. A noise level of 14 % translates into an error for each individual displacement measurement ranging from ±1.1 mm up to ±9.8 mm for measured displacements between 8 mm and 70 mm at the top row, and from 0 mm up to ± 11.1 mm for measured displacements ranging from 0 mm to 80 mm at the arch. Expressing the uncertainty in this way facilitates clearer interpretation for monitoring practitioners.

In the current article, a GA controls the inverse problem solution with Eq. (1) defining the calculation of the mentioned objective function. The GAs are global search metaheuristics particularly well–suited for discrete design variables and discontinuous objective functions. Unlike gradient–based optimization methods, which may struggle with the combinatorial complexity of block configurations, GA does not require gradient information, can effectively navigate multiple local optima, and is robust to measurement noise. These algorithms have been widely applied in structural damage detection problems [54,55], demonstrating both flexibility and reliability in similar contexts.

To this end, FemDem simulations are performed with one or two blocks missing at locations proposed by the GA population, calculating a new set of displacements δ_i^j for each run (where j denotes the GA iteration). Subsequently, the objective function f_v is formulated as the difference between the experimental (or "real") and the GA-generated displacements:

$$f_v = \log\left(\sum_{i=1}^N \left| \left(\delta_i^{ex} - \delta_i^j\right) \right| + 10^{-16} \right),\tag{1}$$

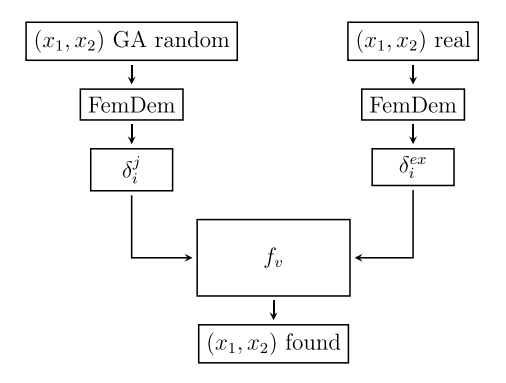


Fig. 5. Flowchart for the computation of the objective function.

where i is the number of the control node (shown in red) of Fig. 1 and N=78 its maximum. The objective function was designed to be both robust against measurement errors and applicable to real monitoring situations. Robustness is achieved through the use of the L1 norm, which reduces the influence of extreme values in the data, a logarithmic transformation f_v to improve optimization convergence [56], normalization of displacement differences to handle variations in measurement scale, and multiple control points to provide redundancy in case of sensor malfunction or data loss. In terms of applicability, the formulation works effectively under static and quasi–static loading conditions but can also be extended to dynamic situations. Its structure allows integration with various sensor types and can be adapted to different bridge geometries and damage scenarios [33].

Fig. 5 summarizes the GA procedure: the algorithm iteratively adjusts the position of the missing block from the population, and FemDem calculates the corresponding vertical displacement δ^j at each control node i.

These displacements are compared with the initial δ^{ex} corresponding to a case with the actual missing block position (unknown to the GA); subsequently, the objective function is evaluated at each step j.

The inverse problem can be posed as a minimization (which can be constrained) that is defined as finding (x_1, x_2) such that:

$$\min_{(x_1, x_2)} f_v(x_1, x_2) \tag{2}$$

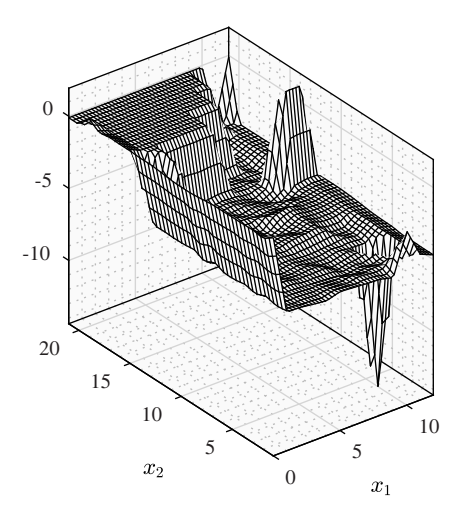
As mentioned, when a single block is missing, the variables to optimize are the positions (x_1,x_2) . The coordinates of the block's center of gravity are stored in a vector using the previously defined indices. For two-block detection cases, the variables are duplicated as (x_1,x_2) and (x_3,x_4) . To proceed with the calculation, GA changes the variables in integer steps within the range of the indices taken from a reduced population.

4. Absence of one block

Fig. 6 illustrates the objective function Eq. (1) for a single missing block, specifically for the (10,4) location in the wall near the bridge's top and upper left corner, calculated without noise. Unlike typical GA cases where only a reduced population is calculated, a population size of 50 is used for this problem, 212 cases are run for this figure, representing the absence of all blocks one by one.

To prevent the algorithm from becoming trapped in local minima near the global minimum and to maintain the genetic diversity of the population, a high mutation and crossover factors of 0.7 and 0.8, respectively, are applied.

Several regions can be identified in the figure. For missing blocks located near (10,4), f_v exhibits a flat profile with minor undulations. This area corresponds to the majority of the left wall, where any missing block produces a displacement field δ^j very similar to the initial δ^{ex} . Thus, the difference in Eq. (5) is nearly uniform and close to zero for all blocks,



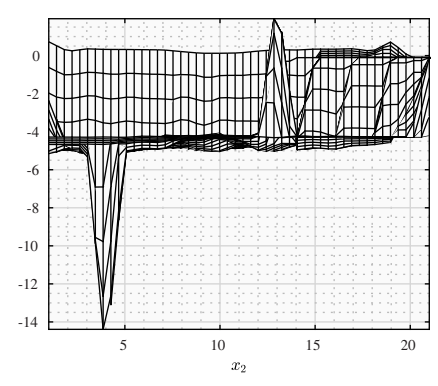


Fig. 6. Objective function without noise of all cases for a missing block at $x_1 = 10$, $x_2 = 4$. Large values truncated for better representation.

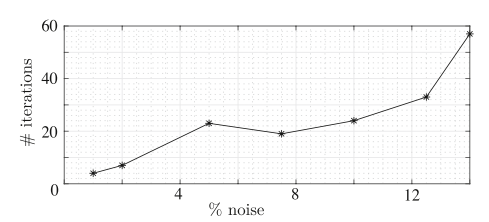


Fig. 7. Noise level versus number of GA iterations to converge for a missing block at (10.4).

and the logarithm of the sum tends to a significant negative value. The function increases as the GA case j moves away from (10,4). Specifically, for missing blocks located at the arch $(x_1=0)$, f_v increases rapidly due to the partial collapse of the structure, which generates large displacements. A similar situation is observed for locations near the bridge's top. A peak close to the minimum corresponds to missing blocks close to the arch; no collapse occurs, but the movements are significant. Finally, the minimum can be easily observed in the figure, right at the missing block location. Since this f_v minimum is isolated, the mathematical prediction of the missing block location is both unique and accurate.

To analyze the influence of noise on the results, the maximum level that the GA can accept without divergence is assessed for the case (10,4). Fig. 7 shows the noise % versus the number of GA iterations required to converge. For levels lower than 5 %, the increase is almost linear; up to 13 %, an almost flat distribution is observed, steeply increasing from 13 % onwards. It is important to note that convergence generation is not a rigorous indicator since it is highly dependent on random variables

Table 2 Number of iterations for convergence, noise function level for several pairs (x_1, x_2) of missing blocks. Cases without convergence are indicated by a hyphen.

x_1	0	6	6	2	2	4	4	8	8	10	10
x ₂	15	4	4	6	6	10	10	12	12	4	12
% noise	10	5	10	5	10	5	10	5	10	10	10
# iter.	8	9	_	27	65	35	_	127	_	67	32

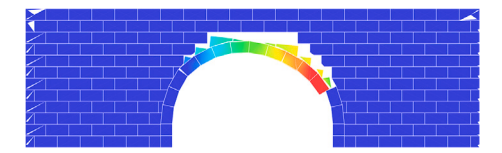


Fig. 8. Bridge vertical displacement field and collapse for missing block (0,15); blocks numbered after the missing block already in movement and contacting the next arch block.

such as the initial population. Nevertheless, it provides an approximate view of how steep the absolute minimum is.

Now, to study the robustness of the inverse problem, the calculation is performed for different missing locations and levels of noise. Table 2 shows the indices (x_1, x_2) of the found missing block location and the iteration at which convergence is reached.

When block (0,15) in the arch is missing, the structure becomes unstable, as large displacements occur at the control nodes close to the keystone (see Fig. 8). In this situation, the missing block can be easily detected in only eight iterations, even for the intermediate—high noise level of 10 %.

For the missing block (6,4), located vertically aligned with (10,4), convergence is strongly influenced by the noise level. While δ^{ex} in the arch remains largely unchanged from the previous case, the top row displacements are significantly perturbed. Fig. 9 (middle) shows that the normalized displacements (with respect to the maximum displacement) above the arch are almost symmetric, a situation confirmed by the symmetry observed in the arch intrados (bottom figure). However, a slight asymmetry is present in the distribution shown in the middle figure, where the δ^{ex} of nodes 1 to 20 is slightly larger than that of nodes 21

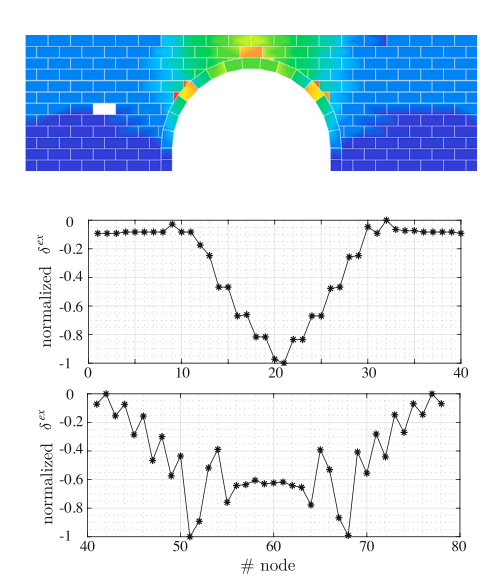


Fig. 9. Vertical displacement field (top) for missing block (6,4) indicated by a white rectangle; noise–free displacements at bridge top (middle) and the external side of the arch (bottom).

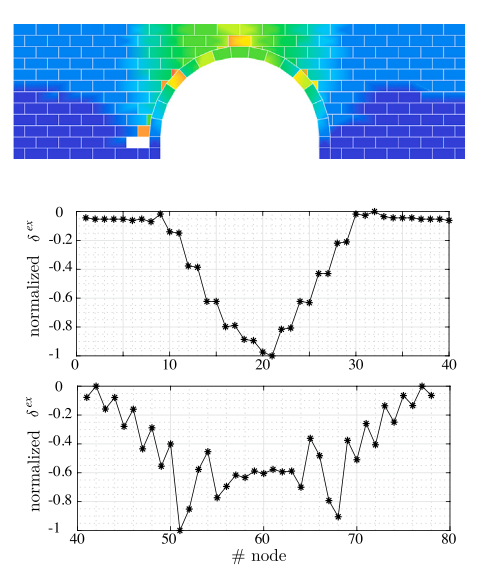


Fig. 10. Vertical displacement field (top) for missing block (2,6) indicated by a white rectangle; noise–free displacements at bridge top (middle) and the external side of the arch (bottom).

to 40. The small perturbation can only be detected with nine iterations for a low noise level of 5 %, but the location is impossible with 10 % as listed in Table 2.

The absence of (2,6) close to the arch bottom left produces relatively large movements in its vicinity. The top Fig. 10 shows that the orange block above (2,6) experiences one of the highest displacements, slightly rearranging the neighboring blocks. This effect is also evident in the small asymmetries depicted in Fig. 10. The largest difference is observed at nodes 10 to 15 in the middle figure, attributed to their vertical alignment with the missing block. Consequently, the sought location can be found with an intermediate number of iterations, even for 10 % noise.

The (4,10) case corresponds to a missing block located symmetrically to the previous example, but slightly farther to the right. The motion of the surrounding area is small and does not produce much rearrangement. The missing block has little influence on the symmetry of the bridge and arch displacements; see the Figs. 11 middle and bottom. However, a small perturbation is observed around the top nodes 31 to 40, where the displacement is slightly smaller than that of their symmetric counterparts (nodes 1 to 10). This perturbation in the arch and top sides enables the detection of the missing spot with a 5 % noise level, but it is undetectable with a higher noise level.

The next case is similar, but involves the missing block (8,12), situated four rows higher and farther from the arch than the previous instance. Therefore, its influence on the arch's displacement field is negligible, as the distribution remains symmetric (Fig. 12 bottom). However, a perturbation is observed at the bridge's top (middle figure), and the number of iterations required for convergence at 5 % noise is higher than in the previous case, while detection is impossible at 10~% noise.

A noteworthy case arises when the missing block is located in one of the uppermost rows of the bridge. If this block is, for instance, (10,4), the situation is shown in Fig. 4. However, if the missing block is close to the keystone (10,12), an asymmetry in this area will appear due to the significant rearrangement close to the gap, Fig. 13 middle. Consequently, the normalized control node distributions at the top and the arch suffer a loss of symmetry, and the detection is achieved with an intermediate number of iterations even with a $10\,\%$ noise.

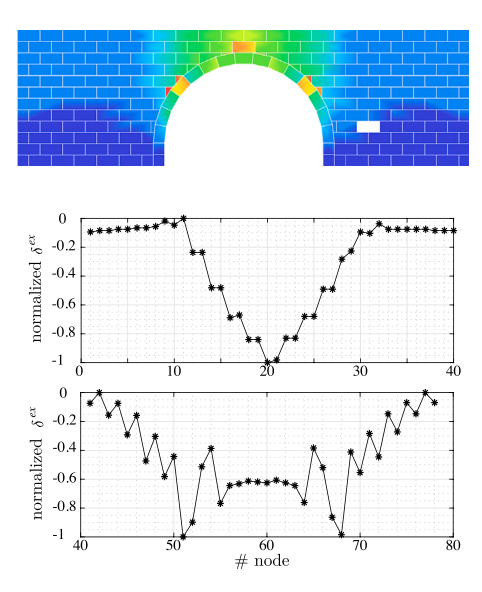


Fig. 11. Vertical displacement field (top) for missing block (4,10) indicated by a white rectangle; noise–free displacements at bridge top (middle) and the external side of the arch (bottom).

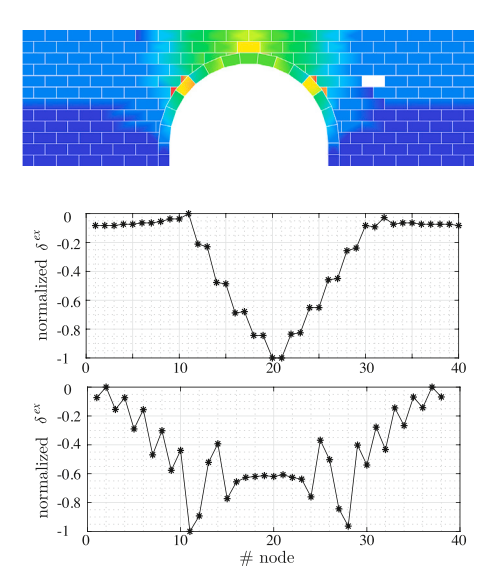


Fig. 12. Vertical displacement field (top) for missing block (8,12) indicated by a white rectangle; noise–free displacements at bridge top (middle) and the external side of the arch (bottom).

5. Absence of two blocks

This section presents a second set of analyses performed to detect two randomly located missing blocks. The same procedure as that of Table 2 is followed to show that the method is consistent and robust. In Table 3, the results for several pairs of missing blocks (x_1, x_2) and (x_3, x_4) are shown, as well as the noise % and the generation for which the GA converges.

From the analysis of the table, it was necessary to reduce the noise level from 10 % to 5 % in all two-block cases, as convergence could not be achieved with the higher value in any instance.

When the first missing block is located in the arch ($x_1 = 0$, first two columns of the table), the position of the second block becomes irrelevant, undetectable, and independent of the noise level. This behavior occurs because the large displacements produced in the arch mask any small perturbations that might occur in other areas. The absence of two

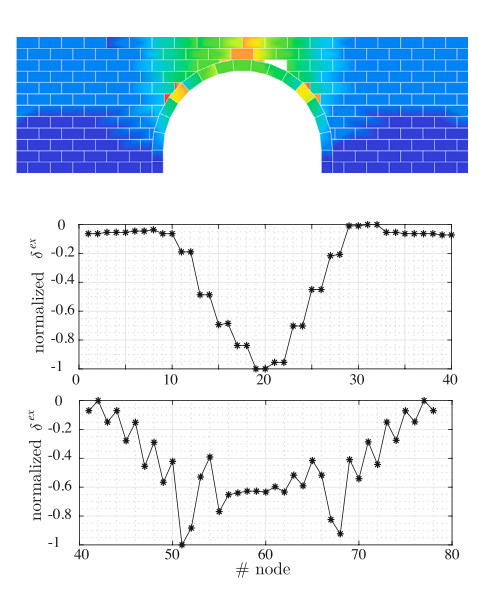


Fig. 13. Vertical displacement field (top) for missing block (10,12) indicated by a white triangle; noise–free displacements at bridge top (middle) and external side of the arch (bottom).

Table 3 Number of iterations for convergence for missing blocks (x_1, x_2) , (x_3, x_4) , as a function of noise level. Cases without convergence are indicated by a hyphen.

6 10
4 12
8 10
1 4
5 5
239 213
239 213
8 1 5 2

blocks approximately located in the same vertical line and away from the arch, case (4,2)+(11,3), produces a noticeable decrease in the top distribution of the left side; see the Fig. 14 middle. This effect is not detected in the arch distribution of Fig. 14 bottom. However, the missing blocks introduce asymmetry in both distributions, particularly in the top left section of the wall. Therefore, the number of iterations to reach convergence is relatively small, even with an intermediate noise level. The displacement field (Fig. 14 bottom) is symmetric in areas near the central arch since the missing blocks are far away.

A substantial local collapse occurs when the missing blocks are contiguous, such as (11,4)+(11,3), leading to the collapse of the blocks above them. Convergence is achieved within an intermediate number of iterations because the displacement is concentrated in this area (see Fig. 15).

If the missing blocks are quasi-symmetric and located near the arch's base, such as (4,10)+(2,6), the number of iterations for convergence is intermediate at low noise levels. The maxima δ^{ex} are concentrated near the block (2,6), see Fig. 16 top, due to the rearrangement near the bottom left side of the arch. Consequently, the asymmetry is easily found in Fig. 16, middle and bottom distributions.

For a missing block in the vicinity of the arch, with the other located on the bridge's left side (e.g., (6,4)+(8,1), figures not shown), the GA identifies the locations within an intermediate number of iterations. This is due to the difficulty of finding the block on the left end, while the one near the arch is easily identified. The number of iterations remains similar across different noise levels, indicating the persistent difficulty in locating the extreme block. A similar behavior is found for cases (10,12)+(10,4), for which one of the blocks is very close to the keystone while the other is at an intermediate distance. The figure is also

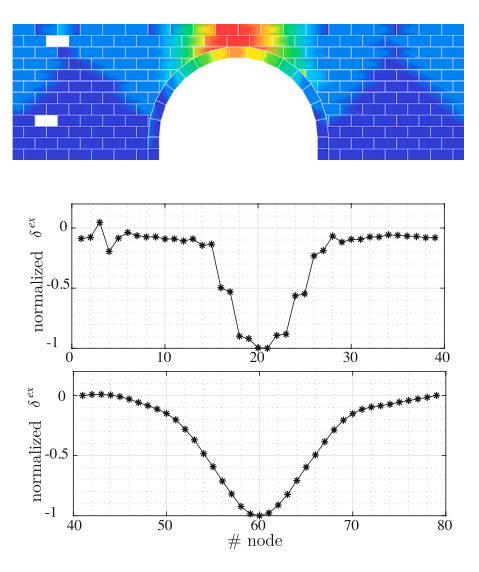


Fig. 14. Vertical displacement field (top) for missing blocks (4,2)+(11,3) indicated by white rectangles; noise–free displacements at bridge top (middle) and external side of the arch (bottom).

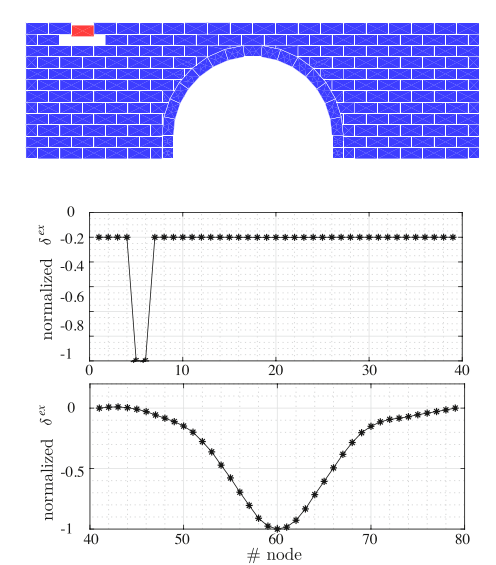


Fig. 15. Vertical displacement field (top) for missing blocks (11,4) + (11,3) indicated by white rectangles; noise–free displacements at bridge top (middle) and external side of the arch (bottom).

not presented, but δ^{ex} are large close to the keystone, and small near the arch on the left.

Generally, blocks in high rows are easier to detect, and GA converges with fewer generations. It is important to note that the number of iterations for convergence depends on random variables and varies slightly for the same simulation run. However, it provides a good idea of how easy or difficult convergence is.

6. Conclusions

The development of a parametric FemDem model enables the characterization of damaged masonry structures, attributable to its capacity to accurately model block interactions. Furthermore, this method is well-suited for implementing inverse problems aimed at damage detection.

To some degree, the bridge displacements under any set of loads depend on the damage position. Missing blocks near the arch produce significant displacements and are therefore easier to detect than those

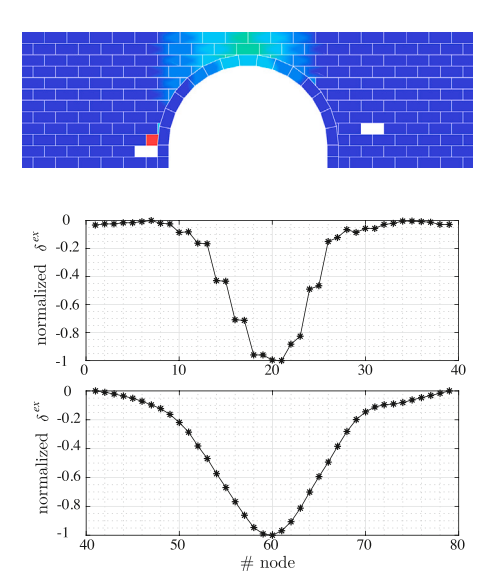


Fig. 16. Vertical displacement field (top) for missing blocks (4,10) + (2,6) indicated by white rectangles; noise–free displacements at bridge top (middle) and external side of the arch (bottom).

caused by damage located in intermediate or remote zones from this arch.

The noise applied to the primary case—used to simulate the experimental data—significantly influences the results. A medium noise level results in damage not detectable for damage located in intermediate or far–off areas from the arch. Similarly, in situations where the damage is in the vicinity of the arch, high noise levels prevent the location of the damage. In other scenarios, the prediction is accurate.

Finally, the statistical variability of the mechanical and geometrical properties of the bridge makes the development of probabilistic inverse problems necessary despite their high computational cost.

Disclosure statement

No potential conflict of interest was reported by the authors.

CRediT authorship contribution statement

R. Bravo: Writing – original draft, Validation, Project administration, Methodology, Investigation, Formal analysis, Conceptualization. **J.L. Pérez-Aparicio:** Writing – original draft, Supervision.

Funding

This investigation has been developed within the framework of the research project: **Grant RTI2018-093621-B-I00**, "Simulación integrada no lineal del comportamiento estructural de puentes ferroviarios de fábrica ante acciones dinámicas y nuevos requerimientos de tráfico", funded by MCIN/AEI/ 10.13039/501100011033 and by ERDF A way of making Europe. The authors wish to express their gratitude for the financial support provided by the aforementioned entities.

Declaration of competing interest

The authors declare that they have no known competing financial interests or personal relationships that could have appeared to influence the work reported in this paper.

References

- Campbell J. Brick: a world history. Thames and Hudson Ltd.; 2003. https://books.google.es/books?id=seh9QgAACAAJ
- [2] Heyman J. The masonry arch. In: Ellis Horwood series in engineering science. 1st Edition ed. E. Horwood; 1982. https://archive.org/details/masonryarch0000heym

[3] Bićanić N, Stirling C, Pearce CJ. Discontinuous modelling of masonry bridges. Comput Mech 2003;31(1):60–8. https://doi.org/10.1007/s00466-002-0393-0

- [4] Rowland ID, Howe TN. Vitruvius: 'Ten books on architecture'. Cambridge University Press; 2001. https://books.google.es/books?id=z22_AwAAQBAJ
- [5] Huerta S. Galileo was wrong: the geometrical design of masonry arches. Nexus Netw J 2006;8:25–52. https://doi.org/10.1007/s00004-006-0016-8
- [6] Suarez FJ, Bravo R. Historical and probabilistic structural analysis of the Royal Ditch Aqueduct in the Alhambra (Granada). J Cult Herit 2014;15(5):499–510. https://doi.org/10.1016/j.culher.2013.11.010. https://www.sciencedirect.com/science/ article/pii/S1296207413002197
- [7] MEXE. Military load classification of civil bridges by reconnaissance and correlation methods, Tech. rep., Military Engineering Experimental Establishment, Christchurch: 1963.
- [8] Castigliano A. Nuova teoria intorno all'equilibrio dei sistemi elastici. Proc R Accad Sci Turin 1875:11(132):127–286.
- [9] Crisfield MA. Numerical methods for the non-linear analysis of bridges. Comput Struct 1988;30(3):637–44. https://doi.org/10.1016/0045-7949(88)90299-4. https://www.sciencedirect.com/science/article/pii/0045794988902994
- [10] Cundall PA, Strack ODL. A discrete numerical model for granular assemblies. Geotechnique 1979;29:47–65. https://doi.org/10.1680/geot.1979.29.1.47
- [11] Lemos JV. Discrete element modelling of masonry structures. Int J Archit Herit 2007;1(2):190–213. arXiv: https://doi.org/10.1080/15583050601176868
- [12] Dimitri R, De Lorenzis L, Zavarise G. Numerical study on the dynamic behavior of masonry columns and arches on buttresses with the discrete element method. Eng Struct 2011;33(12):3172–88. https://doi.org/10.1016/j.engstruct.2011.08.018
- [13] Gonen S, Pulatsu B, Erdogmus E, Lourenço PB, Soyoz S. Effects of spatial variability and correlation in stochastic discontinuum analysis of unreinforced masonry walls. Constr Build Mater 2022;337:127511. https://doi.org/10.1016/j.conbuildmat.2022.127511. https://www.sciencedirect.com/science/article/pii/S0950061822011886
- [14] Colombo C, Savalle N, Mehrotra A, Funari MF, Lourenço PB. Experimental, numerical and analytical investigations of masonry corners: Influence of the horizontal pseudo-static load orientation. Constr Build Mater 2022;344:127969. https://doi.org/10.1016/j.conbuildmat.2022.127969. https://www.sciencedirect.com/science/article/pii/S0950061822016397
- [15] Casapulla C, Portioli F. Experimental and analytical investigation on the frictional contact behavior of 3D masonry block assemblages. Constr Build Mater 2015;78:126–43. https://doi.org/10.1016/j.conbuildmat.2014.12.100. https://www.sciencedirect.com/science/article/pii/S0950061814014020
- [16] Pulatsu B, Erdogmus E, Lourenço PB, Lemos JV, Tuncay K. Simulation of the inplane structural behavior of unreinforced masonry walls and buildings using DEM. Structures 2020;27:2274–87. https://doi.org/10.1016/j.istruc.2020.08.026. https://www.sciencedirect.com/science/article/pii/S2352012420304173
- [17] Bravo R, Perez-Aparicio JL. Discontinuous numerical analysis of masonry vaults. Vol. 3. Berlin: Springer-Verlag Berlin; 2007. pp. 365–80.
- [18] Amirhossein Mehrbod AA, Amirhossein Mehrbod FB, Hashemol-Hosseini H. Seismic vulnerability assessment of stone arch bridges by nonlinear dynamic analysis using discrete element method. Int J Architect Herit 2023;17(11):1791–812. arXiv: https: //doi.org/10.1080/15583058.2022.2071182
- [19] Stefanou I, Psycharis I, Georgopoulos I-O. Dynamic response of reinforced masonry columns in classical monuments. Constr Build Mater 2011;25(12):4325–37, masonry Research and Practice. doi:https://doi.org/10.1016/j.conbuildmat.2010.12. 042. https://www.sciencedirect.com/science/article/pii/S0950061810007336
- [20] Gobbin F, de Felice G, Lemos JV. Numerical procedures for the analysis of collapse mechanisms of masonry structures using discrete element modelling. Eng Struct 2021;246:113047. https://doi.org/10.1016/j.engstruct.2021.113047. https://www.sciencedirect.com/science/article/pii/S014102962101186X
- [21] Suárez FJ, Bravo R, González JA. Structural and constructive analysis of a faux vault, the dome of San Juan de Dios Church, in Granada (Spain). Int J Archit Herit 2021;15(5):728–39. arXiv: https://doi.org/10.1080/15583058.2019.1645242
- [22] Rafiee A, Vinches M, Bohatier C. Modelling and analysis of the nîmes arena and the arles aqueduct subjected to a seismic loading, using the non-smooth contact dynamics method. Eng Struct 2008;30(12):3457–67. https://doi.org/10.1016/j.engstruct. 2008.05.018
- [23] Papa E, Nappi A. Numerical modelling of masonry: a material model accounting for damage effects and plastic strains. Appl Math https://doi.org/10.1016/S0307-904X(97)00011-5. https://www.sciencedirect. com/science/article/pii/S0307904X97000115
- [24] Bayraktar A, Şahin A, Özcan DM, Yildirim F. Numerical damage assessment of Haghia Sophia bell tower by nonlinear FE modelling. Appl Math Model 2010;34(1):92–121. https://doi.org/10.1016/j.apm.2009.03.033. https://www.sciencedirect.com/science/article/pii/S0307904X09000900
- [25] Dolatshahi KM, Aref AJ. Two-dimensional computational framework of mesoscale rigid and line interface elements for masonry structures. Eng Struct 2011;33(12):3657–67. https://doi.org/10.1016/j.engstruct.2011.07.030
- [26] Pérez-Aparicio JL, Bravo R, Ortiz P. Refined element discontinuous numerical analysis of dry-contact masonry arches. Eng Struct 2013;48:578–87. https://doi.org/10. 1016/j.engstruct.2012.09.027. https://www.sciencedirect.com/science/article/pii/ S0141029612005056
- [27] Theodossopoulos D, Sinha B. A review of analytical methods in the current design processes and assessment of performance of masonry structures. Constr Build Mater 2013;41:990–1001. https://doi.org/10.1016/j.conbuildmat.2012.07.095. https:// www.sciencedirect.com/science/article/pii/S0950061812005715
- [28] Munjiza A. The combined finite-discrete element method. John Wiley & Sons, Ltd; 2004. https://doi.org/10.1002/0470020180

- [29] Fukuda D, Mohammadnejad M, Liu H, Zhang Q, Zhao J, Dehkhoda S, et al. Development of a 3D hybrid finite-discrete element simulator based on GPGPUparallelized computation for modelling rock fracturing under quasi-static and dynamic loading conditions. Rock Mech Rock Eng 2020;53(3):1079–112. https: //doi.org/10.1007/s00603-019-01960-z
- [30] Ucgul M, Saunders C, Fielke JM. Comparison of the discrete element and finite element methods to model the interaction of soil and tool cutting edge. Biosyst Eng 2018;169:199–208. https://doi.org/10.1016/j.biosystemseng.2018.03. 003. https://www.sciencedirect.com/science/article/pii/S1537511017309157
- [31] Chen X, Wang H, Chan AHC, Agrawal AK. Dynamic failure of dry-joint masonry arch structures modelled with the combined finite-discrete element method. Computational Particle Mechanics 2020;7(5):1017–28. https://doi.org/10.1007/s40571-019-00297-2
- [32] Smoljanović H, Zivaljić N, Nikolić Z. A combined finite-discrete element analysis of dry stone masonry structures. Eng Struct 2013;52:89–100. https://doi.org/10. 1016/j.engstruct.2013.02.010. https://www.sciencedirect.com/science/article/pii/ S0141029613000655
- [33] Moughty JJ, Casas JR. A state of the art review of modal-based damage detection in bridges: development, challenges, and solutions. Appl Sci 2017;7(5). https://doi. org/10.3390/app7050510. https://www.mdpi.com/2076-3417/7/5/510
- [34] Orbán Z, Gutermann M. Assessment of masonry arch railway bridges using non-destructive in-situ testing methods. Eng Struct 2009;31(10):2287–98. https://doi.org/10.1016/j.engstruct.2009.04.008. https://www.sciencedirect.com/science/article/pii/S0141029609001606
- [35] Soleymani A, Jahangir H, Nehdi ML. Damage detection and monitoring in heritage masonry structures: systematic review. Constr Build Mater 2023;397:132402. https://doi.org/10.1016/j.conbuildmat.2023.132402. https://www.sciencedirect.com/science/article/pii/S0950061823021189
- [36] Verstrynge E, Lacidogna G, Accornero F, Tomor A. A review on acoustic emission monitoring for damage detection in masonry structures. Constr Build Mater 2021;268:121089. https://doi.org/10.1016/j.conbuildmat.2020.121089. https://www.sciencedirect.com/science/article/pii/S0950061820330932
- [37] Ramos LF, De Roeck G, Lourenço P, Campos-Costa A. Damage identification on arched masonry structures using ambient and random impact vibrations. Eng Struct 2010;32(1):146–62. https://doi.org/10.1016/j.engstruct.2009.09.002. https://www.sciencedirect.com/science/article/pii/S0141029609002909
- [38] Pepi C, Cavalagli N, Gusella V, Gioffrè M. Damage detection via modal analysis of masonry structures using shaking table tests. Earthq Eng Struct Dyn 2021;50(8):2077–97. arXiv:, doi:https://doi.org/10.1002/eqe.3431. https://onlinelibrary.wiley.com/doi/pdf/10.1002/eqe.3431. https://onlinelibrary.wiley.com/doi/abs/10.1002/eqe.3431
- [39] Nalon GH, Ribeiro JCL, da Silva RM, Pedroti LG, de Araújo END. Self-sensing concrete masonry structures with intrinsic abilities of strain monitoring and damage detection. Structures 2024;59:105760. https://doi.org/10.1016/j.istruc.2023. 105760. https://www.sciencedirect.com/science/article/pii/S2352012423018489
- [40] Zhou Y, Wang Y, Wang R, Zhang W, Yang H. Automatic crack detection and segmentation of masonry structure based on deep learning network and edge detection. Structures 2025;76:108850. https://doi.org/10.1016/j.istruc.2025.108850. https://www.sciencedirect.com/science/article/pii/S2352012425006642
- [41] Zhu X, Zhu Q, Zhang Q, Du Y. Deep learning-based 3D reconstruction of ancient buildings with surface damage identification and localization. Structures 2025;73:108383. https://doi.org/10.1016/j.istruc.2025.108383. https://www.sciencedirect.com/science/article/pii/S2352012425001973
- [42] Giordano A, Mele E, De Luca A. Modelling of historical masonry structures: comparison of different approaches through a case study. Eng Struct 2002;24(8):1057–69. https://doi.org/10.1016/S0141-0296(02)00033-0. https://www.sciencedirect.com/science/article/pii/S0141029602000330
- [43] Do HQ, Aragón AM, Schott DL. A calibration framework for discrete element model parameters using genetic algorithms. Adv Powder Technol 2018;29(6):1393–403. https://doi.org/10.1016/j.apt.2018.03.001. https://www.sciencedirect.com/science/article/pii/S0921883118300773
- [44] Goldberg DE. The design of innovation: Lessons from and for competent genetic algorithms. In: Vol. 1 of genetic algorithms and evolutionary computation. 1st Edition ed. Springer; 2002. https://doi.org/10.1007/978-1-4757-3643-4
- [45] Chen R, Li J, Qian Y, Peng R, Jiang S, Hu C, et al. An effective inverse procedure for identifying demparameters of rock-like materials. Math Probl Eng 2019;2019:1–13. https://doi.org/10.1155/2019/6969546
- [46] Pérez-Aparicio JL, Bravo R, Gómez-Hernández JJ. Optimal numerical design of bucket elevators using discontinuous deformation analysis. Granular Matter 2014;16(4):485–98. https://doi.org/10.1007/s10035-014-0485-5
- [47] Bravo R, Pérez-Aparicio J. Combined finite-discrete element method for parameter identification of masonry structures. Constr Build Mater 2023;396:132297. https://doi.org/10.1016/j.conbuildmat.2023.132297. https://www.sciencedirect.com/science/article/pii/S0950061823020135
- [48] Sarhosis V, De Santis S, de Felice G. A review of experimental investigations and assessment methods for masonry arch bridges. Struct Infrastruct Eng 2016;12(11):1439–64. arXiv: https://doi.org/10.1080/15732479.2015.1136655
- [49] Zhou Y, Li M, Shi Y, Di S, Shi X. Damage identification method of tied-arch bridges based on the equivalent thrust-influenced line. Struct Control Health Monit 2024;2024(1):6896975. arXiv: https://doi.org/10.1155/2024/6896975. https:// onlinelibrary.wiley.com/doi/pdf/10.1155/2024/6896975
- [50] Sarhosis V, Forgács T, Lemos JV. A discrete approach for modelling back-fill material in masonry arch bridges. Comput Struct 2019;224:106108. https://doi.org/10.1016/j.compstruc.2019.106108. https://www.sciencedirect.com/science/article/pii/S0045794919307084

[51] Pulatsu B, Erdogmus E, Lourenço PB. Simulation of masonry arch bridges using 3D discrete element modelling. In: Aguilar R, Torrealva D, Moreira S, Pando MA, Ramos LF, editors. Structural analysis of historical constructions; Cham: Springer International Publishing; 2019. p. 871–80.

- [52] Lourenco P. Computational strategy for masonry structures, [Ph.D. thesis], Civil Engineering and Geosciences; 1996 Feb. http://resolver.tudelft.nl/uuid:4f5a2c6cd5b7-4043-9d06-8c0b7b9f1f6f
- [53] Vermeltfoort AT, Raijmakers T, Janssen HJM. Shear tests on masonry walls. In: Hamid A, Harris H, editors. 6th North American Masonry Conference, 6-9 June 1993, Philadelphia, Pennsylvania, USA; Technomic Publ. Co.; 1993. p. 1183–93.
- [54] Alves VN, de Oliveira MM, Ribeiro D, Calçada R, Cury A. Model-based damage identification of railway bridges using genetic algorithms. Eng Fail Anal 2020;118:104845. https://doi.org/10.1016/j.engfailanal.2020.104845. https://www.sciencedirect.com/science/article/pii/S1350630720306580
- [55] Tiberti S, Grillanda N, Mallardo V, Milani G. A genetic algorithm adaptive homogeneous approach for evaluating settlement-induced cracks in masonry walls. Eng Struct 2020;221:111073. https://doi.org/10.1016/j.engstruct.2020.111073. https://www.sciencedirect.com/science/article/pii/S0141029620321040
- [56] Gallego R, Rus G. Identification of cracks and cavities using the topological sensitivity boundary integral equation. Comput. Mech. 2004;33(2):154–63. https://doi.org/10.1007/s00466-003-0514-4